HHS Public Access

Author manuscript

Nat Methods. Author manuscript; available in PMC 2013 October 28.

Published in final edited form as:

Nat Methods. ; 8(10): 871–878. doi:10.1038/nmeth.1694.

Miniaturized integration of a fluorescence microscope

Kunal K. Ghosh[1,2,*], **Laurie D. Burns**[2,*], **Eric D. Cocker**[2,*], **Axel Nimmerjahn**[2], **Yaniv Ziv**[2], **Abbas El Gamal**[1], and **Mark J. Schnitzer**[2,3,4]

[1]David Packard Electrical Engineering Building, Stanford University, Stanford CA 94305, USA

[2]James H. Clark Center, Stanford University, Stanford CA 94305, USA

[3]Howard Hughes Medical Institute, Stanford University, Stanford CA 94305, USA

[4]CNC Program, Stanford University, Stanford CA 94305, USA

Abstract

The light microscope is traditionally an instrument of substantial size and expense. Its miniaturized integration would enable many new applications based on mass-producible, tiny microscopes. Key prospective usages include brain imaging in behaving animals towards relating cellular dynamics to animal behavior. Here we introduce a miniature (1.9 g) integrated fluorescence microscope made from mass-producible parts, including semiconductor light source and sensor. This device enables high-speed cellular-level imaging across ~0.5 mm^2 areas in active mice. This capability allowed concurrent tracking of Ca^{2+} spiking in >200 Purkinje neurons across nine cerebellar microzones. During mouse locomotion, individual microzones exhibited large-scale, synchronized Ca^{2+} spiking. This is a mesoscopic neural dynamic missed by prior techniques for studying the brain at other length scales. Overall, the integrated microscope is a potentially transformative technology that permits distribution to many animals and enables diverse usages, such as portable diagnostics or microscope arrays for large-scale screens.

Introduction

Modern understanding of technology recognizes miniaturized integration as a pivotal advance that facilitates low-cost production and typically leads to improved performance

Correspondence should be sent to M.J.S. (mschnitz@stanford.edu).

*Author Contributions. These authors contributed equally.

*K.K.G. performed optical analysis, designed electronic circuits, assembled microscopy systems, wrote cell-counting software, and performed the zebrafish, tuberculosis, and cell counting experiments.

*LDB performed optical analysis, designed the optical pathway, assembled microscopy systems, performed cerebellum and hippocampal imaging studies, and analyzed the Ca^{2+}-imaging data.

*E.D.C. designed the mechanical housing, heat dissipation, focusing mechanisms, and illumination control circuitry, assembled microscopy systems, designed and built behavioral enclosures with video acquisition, and analyzed the behavioral and microcirculation data. A.N. developed the cerebellar preparation and performed cerebellar imaging studies. Y.Z. developed and performed the hippocampal imaging methodology. A.E.G. supervised the project. M.J.S. supervised the project and wrote the paper. All authors designed experiments and edited the paper.

The authors report competing financial interests. K.K.G., E.D.C., A.E.G. and M.J.S. have equity in a company (Inscopix) pursuing imaging applications based on the integrated microscope.

CFI Statement: K.K.G., E.D.C., A.E.G. and M.J.S. have equity in a company (Inscopix) pursuing imaging applications based on the integrated microscope.

and unanticipated applications[1]. Such impact has been shown in diverse arenas including telecommunications, computing, and genomics. One technology that has largely resisted integration is the light microscope, which generally remains a bulky and costly tabletop instrument. In neuroscience, microscopy has achieved widespread usage in live animals, but the limitations of conventional microscopes hamper the scope and scale of brain-imaging experiments[2]. Towards improving the accessibility, quality, and throughput of brain-imaging studies in freely behaving mice, we created a miniature, integrated fluorescence microscope with a design permitting mass-production and high-speed tracking of neural dynamics. The microscope is based on micro-optics and semiconductor optoelectronics, both readily mass fabricated, and integrates all optical parts within a tiny package easily held by the fingertips. Compared to high-resolution fiber-optic microscopes, our device offers advantages regarding optical sensitivity, field of view, attainable resolution, mechanical flexibility for the animal, cost, and portability.

Previous methods for microscopy in behaving animals required tabletop optical instrumentation that could not be readily distributed to many mice in parallel[2-9]. Some methods also required head-fixation of the animal[4,5,8,9], which is incompatible with standard rodent behavioral assays. Our microscope clears both these challenges, is 1.9 g in mass, and can be carried by an adult mouse on its head. Electrical wires carry power, control signals, and data to and from the animal, but these are sufficiently fine to permit a highly flexible mechanical connection. This is unlike fiber-optic microscopes, which are prone to exerting torque on the animal due to the finite bending radius of optical fiber.

We explored the integrated microscope's capabilities for brain-imaging by visualizing cerebellar microcirculation across different locomotor behaviors. The ∼500% increase in optical throughput over our prior fiber-optic microscope[6] sufficiently improved data quality that we could analyze capillary diameters and flow speeds with seconds-scale resolution, rather than averaging over behavioral epochs[6]. Although we had expected capillaries across the imaging field would be regulated uniformly, only a spatially scattered minority of vessels significantly changed diameters and flow speeds as the animal switched from resting to active behaviors. Capillary regulation may thus have unanticipated precision at the tens of microns scale.

We also tracked Ca^{2+} spiking in up to 206 individual cerebellar Purkinje neurons, ∼700% more than with our fiber-optic microscope[6]. The improved throughput implied our recordings required lower illumination power and lasted up to <1 hr without noticeable photobleaching. These improvements led to far larger Ca^{2+} spiking data sets, enabling the initial analysis in freely behaving animals of higher-order spiking correlations among Purkinje neurons. This revealed synchronized Ca^{2+} spiking that arose during motor behavior within individual cerebellar microzones.

Beyond brain imaging, there has been considerable recognition of new applications that would be enabled by miniaturized integration of the light microscope, particularly portable, image-based diagnostics and high-throughput screening[10]. Past efforts to address these have yielded miniaturized devices that needed accessory, conventional optical

instrumentation[11,12] or that did not permit fluorescence imaging and made specialized assumptions about the specimen[13,14].

To illustrate potential usages of the integrated microscope in biotechnology, we show our device permits fluorescent cell counting, for which conventional instruments have substantial footprints and cost. Regarding diagnostics, we show our microscope can detect tuberculosis bacilli in a fluorescence assay. The microscope's portability, potential low cost, and simple electronics requirements should aid dissemination to locations inhospitable to conventional microscopy.

Results

Optical design

The microscope's design exploits recent advances in optoelectronics that have yielded inexpensive but high quality parts, including tiny but bright light-emitting diodes (LEDs) and complementary metal-oxide-semiconductor (CMOS) image sensors with fine pixel sizes and high sensitivity[15]. This allowed us to incorporate all optical parts within a ∼2.4 cm^3 housing (Fig. 1a) (**Online Methods**)

A blue LED resides on a custom 6 mm × 6 mm printed circuit board (PCB). A drum lens collects the LED's emissions, which then pass through a 4 mm × 4 mm excitation filter, deflect off a dichroic mirror, and enter the imaging pathway (Fig. 1b). A gradient refractive index (GRIN) objective lens focuses illumination onto the sample. Fluorescence from the sample returns through the objective, the dichroic, an emission filter, and an achromatic doublet lens that focuses the image onto a CMOS sensor (640 × 480 pixels; 60% quantum efficiency at 530 nm) mounted on a custom 8.4 mm × 8.4 mm PCB (Fig. 1b). The housing, made in polyether-etherketone, permits focusing to sub-micron accuracy by adjusting the camera position. Nine electrical lines (seven connecting to the sensor and two to the LED) carry power, control signals and image data (Fig 1c). An intermediary PCB between microscope and computer coordinates data acquisition and allows full-frame imaging at 36 Hz, or 100 Hz over 300 × 300 pixel sub-regions (Fig. 1c). The maximum field of view is 600 μm × 800 μm, the optical magnification is ∼5.0×, and the lateral resolution is ∼2.5 μm (Table 1). This resolution represents the Nyquist limit set by the camera's 5.6 μm pixel pitch, not the optical limit of the lens design. As CMOS sensors improve, the optical pathway will support ∼1.5 μm resolution (Table 1).

Compared to our fiber-bundle microscope for use in behaving mice[6] the integrated microscope has major advantages (Table 1). Fiber-bundles restrict resolution according to their density of optical fibers, which in turn is capped by light leakage between the individual fibers. The integrated microscope also offers ∼700% greater field of view, ∼500% greater transfer efficiency of fluorescence between the specimen and image detection planes, superior freedom of movement for the mouse due to the floppy tether, vastly improved cost structure due to the reliance on optoelectronics in the single dollar range, and a much smaller and more portable system that does not need optical realignment when transported. As with resolution, the optical design permits further gains in field of view (up to ∼1.15 mm) as CMOS sensors progress. Microscopes based on fiber-bundles are

restricted in field of view by the maximum diameter and bending radius of the bundle an animal can tolerate while behaving naturally. The integrated microscope's control and data lines carry digital signals, so there is no decline in signal quality for long wires allowing slack in the animal's tether. Analog fluorescence signals ported in fiber-optics suffer increased absorption and leakage or crosstalk in fibers of greater length.

Finally, with the integrated microscope all optical parts lie in the animal's reference frame, which substantially improves data quality. In our prior work[6], light source and camera were in the laboratory frame, hence we used a commutator so the fiber could swivel, allowing the mouse to move freely. The illumination field thus rotated in real-time at the specimen plane, and the analysis had to disentangle the spinning illumination from signals within the specimen. Our use of a Hg-arc lamp[6], far more prone to high-frequency fluctuations than the LED employed here, compounded the challenge. The integrated microscope obviates these problems entirely, removing a non-stationary noise source that depended on the mouse's behavior.

Imaging microcirculation in active mice

We first assessed the microscope's performance in live animals by imaging cerebral microcirculation in behaving mice ($n = 7$ mice) (Supplementary Video 1). We focused on lobules V and VI of the cerebellar vermis (Fig. 2a,b), areas implicated in coordinating hind- and forelimbs[16-18]. Bulk hemodynamic responses in cerebellar cortex arise during motor behavior[9,19], but individual capillaries' responses have not been studied.

The integrated microscope's sensitivity and image quality allowed us to track erythrocyte speeds and capillary diameters with 2-s time-resolution. This is in contrast to the averaging over minutes of data for capillaries studied by fiber-optic microscopy[6]. We classified epochs into three behavioral states: periods when the mouse rested; walked about its enclosure; or ran on an exercise wheel (Fig. 2c,d). Motion artifacts were barely apparent, typically < 1 μm even during running (Supplementary Video 1). This is substantially less than motion artifacts during two-photon microscopy in head-fixed behaving animals[4,5,9]. The robustness reported here is likely due to the coupled motion of the cranium and the full optical pathway, and our microscope's faster frame rate and greater depth of field.

Detailed analysis focused on a subset of mice and revealed both locomotor states evoked increases in flow speeds (running: +83 ± 20 μm/s; walking: +21 ± 11 μm/s; mean ± s.e.m;) and capillary diameters (running: +0.52 ± 0.12 μm; walking: +0.27 ± 0.08 μm) compared to resting periods (Fig. 3) (**Online Methods**). These changes were significant ($n = 3$ mice; 97 vessel locations; $P = 10^{-4}$–10^{-3}; Wilcoxon signed rank tests), except for flow speed changes evoked by walking ($P = 0.13$).

We had expected all capillaries within a field of view would uniformly undergo increased speeds and diameters during locomotion. Surprisingly, only a spatially scattered ∼25-30% of capillaries exhibited substantial up-regulation of erythrocyte speeds and vessel diameters (Fig. 3). This indicates capillaries separated by only tens of microns are controlled non-uniformly and that a subset of vessels appears to dominate bulk effects. Future use of the integrated microscope may help identify mechanisms underlying this unexpected precision

in vessel regulation, pertinent to both cerebrovascular disorders and functional brain imaging.

Purkinje neuron Ca^{2+} dynamics and pairwise correlations

We next studied dendritic Ca^{2+} spiking by Purkinje neurons in the cerebellar vermis of behaving mice. These spikes represent the Ca^{2+} component of complex (Na^+ and Ca^{2+}) action potentials[4,6,20] thought to be crucial for cerebellar motor learning[21]. Following injection of the cell-permeant fluorescent Ca^{2+}-indicator Oregon-Green-BAPTA-1-AM into cerebellar cortex, the integrated microscope could record Ca^{2+} spiking from up to 206 individual neurons at frame rates up to 46 Hz (n = 4 mice) (Fig. 4a,b).

We used established computational methods to identify individual Purkinje neurons and extract their Ca^{2+} activity traces from the image data[4] (Online Methods). The identified cells and their spike rates were consistent with anatomical and electrophysiological attributes of Purkinje neurons in mice and prior *in vivo* Ca^{2+}-imaging studies[4,6,20,22] (Fig. 4). As previously, cross-correlograms of Ca^{2+} spiking activity revealed spatial clustering of neurons into local microzones of 7-36 cells with significant pair-wise synchrony[4,22] (Fig. 4c). Microzones are basic cerebellar divisions, each mapped to a specific body part[23], and up to nine microzones were present in individual recordings. After classifying the mouse's behavior into periods of rest, grooming, locomotion, or other behavior (**Online Methods**), we observed that microzones maintained stable identities across different behaviors[4] and showed stronger correlations with cells in neighboring versus distal microzones (Fig. 4c).

In a detailed analysis of n =3 mice, we found that most cell pairs lying within the same microzone were significantly correlated during both rest [84% of n = 3,985 pairs had $P < 0.01$, likelihood ratio test; $P = 4 \cdot 10^{-4} \pm 10^{-3}$ (mean ± s.d. of the significantly correlated pairs)] and locomotor behavior [98% of n = 3,985 pairs had $P < 0.01$; $P = 6 \cdot 10^{-5} \pm 5 \cdot 10^{-4}$ (mean ± s.d.)]. By comparison, only 9% of n = 21,434 cell pairs in distinct microzones were significantly correlated during rest ($P = 2 \cdot 10^{-3} \pm 3 \cdot 10^{-3}$ for the significantly correlated pairs), which rose to 19% ($P = 1 \cdot 10^{-3} \pm 2 \cdot 10^{-3}$) during locomotion. Correlation coefficients for the intrazone cell pairs rose from $r = 0.12 \pm 0.004$ (mean± s.e.m) during rest to $r = 0.21 \pm 0.004$ during locomotion ($P = 10^{-50}$, Wilcoxon signed rank test). Correlation coefficients for interzone pairs were much smaller during both behaviors ($r = 0.01 \pm 0.001$, rest; $r = 0.02 \pm 0.001$, locomotion; n = 21,434 pairs), but slightly higher for cell pairs from adjacent microzones ($r = 0.03 \pm 0.001$, rest; $r = 0.06 \pm 0.001$, locomotion; n = 6,314 pairs).

Behaviorally evoked microzone activation

The large sets of Purkinje neurons and ∼3,500% more spikes collected in our data sets than previously[6] enabled the first analysis of higher-order correlations in these cells' dynamics in freely behaving animals. We found that predominantly during motor activity large cohorts of up to > 30 Purkinje neurons within individual microzones fired synchronous Ca^{2+} spikes (Fig. 5a,b). We used two alternative definitions of synchrony to characterize a microzone's collective activation: either > 35% or > 50% of visible neurons within a microzone were required to spike within a 50 ms interval.

Using either definition and in all behavioral conditions, microzone activation arose far above (~10^5-10^{10}) expected rates due to chance given cells' individual spike rates. Whereas cells' mean spike rates during locomotion rose to 240 ± 10% (s.e.m.) of the resting value (n = 336 cells; $P = 2 \cdot 10^{-52}$, Wilcoxon signed rank test), the rate of microzone activation during locomotion (with > 50% of a microzone's cells spiking together) rose to 810 ± 120% of the resting value (n = 16 microzones; $P = 5 \cdot 10^{-4}$) (Fig. 5c,d). During grooming behavior the increases were less pronounced but still highly significant. Cells' mean spike rates during grooming rose to 160 ± 10% (s.e.m.) of the resting value (n = 336 cells; $P = 3 \cdot 10^{-29}$, Wilcoxon signed rank test), whereas the rate of microzone activation rose to 350 ± 80% of the resting value (n = 16 microzones; $P = 10^{-3}$, Wilcoxon signed rank test) (Fig. 5c,d).

These analyses of microzone activation are based on a conservative overestimate of the synchronized activity during rest, since we did not classify very brief or slight movements as occurring during movement periods. The videos often revealed subtle movements of the mouse accompanying synchronized Ca^{2+} activity that arose during periods classified as rest. During continuous motor behavior, microzone activation represented a substantial fraction of all Ca^{2+} spikes; the cells' median percentage of spiking activity that occurred during microzone activation was as great as > 20% (Fig. 5e).

In vitro applications

Beyond imaging in live animals, the integrated microscope is likely an enabling technology for a range of *in vitro* applications. These might involve portable fluorescence assays, high-throughput screens, imaging inside other instruments such as incubators, or combinations with other integrated components such as microfluidic or gene chips[10].

To initiate exploration we created an array of four integrated microscopes (Supplementary Fig. 1a). We examined wildtype zebrafish intermingled with *erbb*3 mutants, which have deficits in nerve myelination in the peripheral but not the central nervous system[24,25]. Images taken by the microscope array clearly distinguished the mutant fish by their absence of the posterior lateral line nerve and dorsal nerve roots (Supplementary Fig. 1b). These data provide proof-of-concept evidence that arrays of integrated microscopes might underlie parallel screening strategies. Today, image-based screening is often done serially on a conventional microscope[26], which may be unsatisfactory for large sample sets or samples needing continuous monitoring.

We also explored if an array of microscopes might facilitate cell-counting in 96-well plates. Commercial counters often use imaging to count plated cells[27,28] and range in size from benchtop to floor-standing instruments. We tested if our array allowed accurate counting by using live samples of MCF7 cancer cells fluorescently labeled with carboxyfluorescein. Across ~2.5 orders of magnitude in cell density, the microscope array and an image segmentation algorithm gave counts accurate to 4–16% (s.e.m.) (Supplementary Fig. 1c,d), comparable to commercial counters using digital imaging[29].

Other future applications may involve diagnostics. Using auramine-O, a fluorescent marker of tuberculosis (TB) bacilli[30], the integrated microscope readily distinguished TB positive

and negative culture samples (Supplementary Fig. 1e). The microscope's alignment-free portability suggests assays of this type might be tractable in the field.

Discussion

A few prior studies have explored *in vivo* cellular imaging in unrestrained animals but used fiber-optics and benchtop instrumentation not conducive to mass-production[3,6,7]. By comparison, our microscope's composition from mass-producible components should also help promote its dissemination. The LED, image sensor, filters, and microlenses are all made via batch fabrication, so their costs per microscope decline rapidly with production volume. The microscope housings were machined, but these could be molded to facilitate greater volumes, with the cost dominated by the initial mold. Overall, we expect costs per microscope to fall substantially with volume manufacturing. This is not the case with conventional high-resolution microscopes, for which multiple parts still resist batch-fabrication.

Other aspects of the integrated microscope that should aid dissemination include the energy efficiency of LED illumination and the microscope's ease of transport without need for re-alignment. We made seven identical copies of the microscope in the initial production round. These devices contain all optical parts but require a computer and are not standalone. Future, standalone versions should be possible and could benefit in-the-field diagnostics, which demand a high degree of portability.

Creation of the integrated microscope capitalized on recent advances in LEDs and image sensors, but the main innovation was in the system design. We created a miniaturized optical pathway, a data acquisition system, three circuit boards, and a housing with fine focusing capability, while keeping the microscope to 1.9 g mass. Prior approaches to fluorescence imaging in miniaturized format have generally required accessory, tabletop optical instrumentation[6,11,12,31]. An earlier integrated system for use in mobile rats exhibited a Nyquist resolution of ∼20 μm, insufficient for observing individual cells[32]. Optofluidic chips have been incompatible with fluorescence contrast and required assumptions about the specimen, such as that it was flowing at certain speeds at zero optical working distance[13]. Lensless approaches do not produce direct images but involve deciphering diffraction patterns produced by cells immobilized at a fixed working distance[14]. Due to its fluorescence capability, lack of ancillary optical instrumentation, alignment-free portability, and suitability for volume production, the integrated microscope differs from prior miniaturized devices and can address distinct applications, including imaging the dynamics of hundreds of individual neurons in behaving animals.

The integrated microscope will permit Ca^{2+} imaging in deep brain areas of behaving mice when it is combined with recently developed methods for time-lapse micro-optical imaging[33], genetically encoded Ca^{2+}-indicators that are non-ratiometric[34], and an accessory microendoscope to access deep tissues[6,33],. To illustrate, we performed Ca^{2+}-imaging in hippocampal area CA1 of active mice using a GCaMP3 Ca^{2+}-indicator[34] genetically targeted to pyramidal neurons (Supplementary Fig. 2). These studies revealed prominent

Ca^{2+} transients that likely correspond to action potential bursts, as GCaMP3 is not sufficiently sensitive to report single action potentials in these neurons[34].

These proof-of-concept data show neuronal Ca^{2+}-imaging during naturalistic mouse behavior is not restricted to studies of cerebellar cortex. Brain areas where cellular-level epi-fluorescence imaging has worked well in behaving rodents include cerebellum[6], olfactory bulb[35], hippocampus[33,36], and neocortex[37]. Ca^{2+}-imaging should be similarly feasible in various other brain regions. Many institutions are investing in rodent behavioral facilities, and the integrated microscope appears compatible with widely used assays including fear conditioning, novel object recognition, tests of rodent social interaction, or assays involving olfactory cues or foraging for rewards. This flexibility should help add a brain-imaging component to behavioral research using instrumentation that could be less costly, sizable, and challenging to operate than current optical apparatus.

In comparison to two-photon microscopes used to study alert, head-restrained rodents[4,5,8,9], the integrated microscope provides broader fields of view and decreased susceptibility to motion artifacts due to its greater depth of field and faster frame rates (Supplementary Video 1). For comparison, two-photon microscopy in behaving mice allowed tracking of ∼100 Purkinje neurons' Ca^{2+} spiking at < 12 Hz frame rates[4,5,9]; the integrated microscope monitored 206 Purkinje neurons at 46 Hz (Fig. 4). Two-photon microscopy has other virtues, including optical sectioning, lower background fluorescence, superior resolution, and greater robustness to scattering. These are key advantages for imaging cells multiple scattering lengths from the objective lens. However, the pixel dwell times in two-photon microscopy (∼0.1–3 μs) are so brief relative to one-photon imaging frame-rates that in moderate light scattering regimes neuronal Ca^{2+}-spikes are approximately equally detectable in either modality, since the greater photon counts and less severe photon shot noise in one-photon imaging can compensate for this modality's lesser contrast (B. Wilt, J. Fitzgerald, and M.J Schnitzer, *unpublished calculations*).

The two modalities also appear complementary regarding rodent behavioral assays. The integrated microscope permits free-ranging behavior, whereas head-fixation of an animal for two-photon microscopy seems incompatible with many naturalistic behaviors, even with virtual reality methods. However, other behavioral studies should benefit from head-fixation, since it can restrict and simplify behavioral responses. Still, head-fixation seems likely to evoke greater stress responses than naturalistic behavior with a head-mounted device. We expect future roles for both two-photon and integrated microscopy in brain imaging.

We observed synchronization of up to > 30 Purkinje neurons, but selectively during motor behavior and spatially organized by microzone boundaries. Although ∼50–100 μm wide in the medial-lateral dimension, microzones extend millimeters in the rostral-caudal dimension[23], suggesting that during microzone activation hundreds to thousands of Purkinje neurons could be acting simultaneously with the ∼600-μm long subsets observed via the integrated microscope. Such concerted activity of large neural ensembles at the millimeter-scale has few if any precedents. Imaging studies have typically lacked either the resolution of individual neurons' spikes, or the field of view required to observe mesoscale

synchronization. During animal inactivity, individual Purkinje neurons exhibit ongoing Ca^{2+} spiking, whereas the ensemble activation stops or persists at a much-reduced rate. These observations prompt many questions regarding the extent and mechanisms of the large-scale synchronization, the information encoded, and its role in motor behavior.

Neurophysiologic control of motor behavior likely involves large neuronal ensembles acting in an organized fashion. Each microzone is mapped to part of the body plan[23], and coherent microzone activation may carry signals of especial importance for control of this part. The prominence of the microzone's ensemble activation likely enhances its detection and downstream impact in the deep cerebellar nuclei, the sole recipients of Purkinje neuron output from the vermis.

An attractive possibility is that microzone activation provides a means for reliably encoding motor errors in the presence of ongoing Ca^{2+} spiking. Purkinje neurons' Ca^{2+} spikes are driven by climbing fiber axons from the inferior olive, an area where excitatory neurons can synchronize via gap junction networks[23] and are thought to convey motor error information to cerebellar cortex. As our and prior recordings[4,6,38] show, individual Ca^{2+} spikes persist in the absence of body movement and so seem unlikely to signal motor errors in a straightforward way. Ensemble activation of the microzone is nearly exclusive to movement periods and could provide a motor error signal that is readily identifiable against individual cells' baseline spike rates. Beyond the cerebellum, large-scale synchrony in mesoscale neuronal ensembles could be a fundamental means in the brain to reliably engage downstream circuitry and evoke animal behavior.

In addition to its usages in behaving animals, the integrated microscope is a multipurpose instrument for epi-fluorescence imaging. For *in vitro* applications, the microscope has the potential to enable large-scale parallelism, allow imaging inside other instrumentation such as incubators, and reduce costs. Moreover, a high-resolution microscope that can be held by the fingertips and readily ported should stimulate new imaging applications in biology, including portable usages where microscopy is presently challenging or infeasible. In our personal experience, we have found the integrated microscope with its laptop computer can be easily transported on commercial air flights and immediately used at the remote destination. This opens up possibilities for mobile assays, such as for ecological studies or biomedical diagnostics of potential significance for developing nations.

As our cell counting assays show, the integrated microscope can attain counting accuracies comparable to flow cytometry or conventional instrumentation based on digital imaging. Our array of four microscopes points the way to larger arrays that could enable massively parallel strategies for high-content screening. Today, most image-based screens involve one or a few microscopes for serial inspection that ultimately limit throughput. Currently available massively parallel approaches generally do not involve imaging and use simpler screening criteria. When combined with computational tools for analyzing massive data sets, arrays of integrated microscopes might combine the best of high-content screening and massive parallelism. For instance, screens involving high-speed Ca^{2+}-imaging in neurons or myocytes are generally prohibitive today with conventional plate readers but should be feasible with an array of integrated microscopes. For screens requiring diffraction-limited

resolution, it should be straightforward to substitute the existing micro-objective with one designed for diffraction-limited imaging[39].

Integrated technologies usually advance rapidly, which motivated our choice of a design that can capitalize on upcoming sensor advances to improve resolution, sensitivity, and dynamic range. Multi-color imaging should also be feasible. Since CMOS technology underpins most modern electronics, 'intelligent' integrated microscopes seem likely to emerge with sensors having built-in electronic capabilities to facilitate analysis, screening, data compression, or diagnostic evaluations.

Online Methods

Microscope design

We made seven microscopes of identical design that were ∼8.4 mm × 13 mm × 22 mm and 1.9 g in mass. We performed optical ray tracing design studies using ZEMAX software (ZEMAX Development Corporation) and mechanical design using AutoDesk Inventor software (AutoDesk Inc.). We simulated image acquisition by computationally propagating rays emitted from scenes of virtual specimens through the imaging optics in Zemax. ISET software (ImagEval) simulated the acquisition of the resulting images on a virtual model of the image sensor.

Illumination pathway

Each microscope had a blue light-emitting diode (LED) with ∼470 nm spectral peak (Philips LumiLeds, LXML-PB01-0023). The LED resided on a custom 6 mm × 6 mm printed circuit board (PCB) equipped with a heat sink. A drum lens (Edmund Optics, NT45-549) collected illumination light, which then passed through a fluorescence excitation filter (Semrock, bandpass filter, 480/40 nm, 4 mm × 4 mm × 1.05 mm) and reflected off a dichroic mirror (Semrock, FF506-Di02, 4 mm × 4.8 mm) that directed the illumination into the objective lens (see *Imaging pathway*) and to the specimen.

Each LED received power from an external programmable constant current source or a digital pulse-width-modulation-based current source (Supertex Inc., CL330). We calibrated each microscope's LED to determine the illumination power delivered to the specimen over a range of drive currents. The illumination power varied with the temperature of the LED's active element, with observable changes in illumination arising from ∼1 C° variations. Power declines of ∼10% were apparent during the first 60 s after LED activation, but the illumination output stabilized as the LED reached an equilibrium temperature. The voltage drop across the LED's terminals provided a good approximation of the active element's temperature. By using the input current level and the measured LED voltage drop, we estimated the output power to within ±0.5%.

Imaging pathway

A 2-mm-diameter gradient refractive index (GRIN) objective (GRINTech GmBH, GT-IFRL-200, 0.245 pitch length, 0.45 NA) collected fluorescence emissions, which then passed through the dichroic mirror and an emission filter (Semrock, bandpass filter, 535/50

nm, 4 mm × 4 mm × 1.05 mm). An achromatic lens (Edmund Optics, NT45-207, f=15 mm) focused the fluorescence image onto the CMOS image sensor (Aptina Imaging, MT9V021). The magnification was 4.5–5.5×, depending on the focal position. The on-axis, lateral spatial resolution of the optical design was ∼1.2 μm, as estimated by the FWHM of the computed point-spread function. The resolution degraded to ∼1.6 μm at the periphery of the field of view. The size of the pixels on the CMOS sensor (5.6 μm × 5.6 μm) limited the resolution of the acquired images, which we empirically estimated as ∼2.5-2.8 μm by imaging a Siemens Star resolution test pattern[36]. The working distance of the specimen plane from the external face of the objective lens was 150-200 μm, depending on the focal plane. The field of view area ranged from 650 μm × 490 μm to 800 μm × 600 μm.

Mechanical design

Each microscope housing was made of black Polyetheretherketone (PEEK), which is lightweight, chemically resistant, stiff, and machinable. A threaded interface between the CMOS imager housing and microscope body allowed fine adjustment of the spacing between the two, which in turn set the specimen plane that was in focus in the acquired image. A removable filter cover allowed the filter and dichroic to be easily cleaned or exchanged.

CMOS image sensor

The CMOS camera chip (Aptina Imaging, MT9V021) used for image acquisition had 640 × 480 pixels, each 5.6 μm × 5.6 μm. The packaged sensor was 5.8 mm × 5.6 mm. We empirically characterized the sensor to determine its specifications (Supplementary Table 1). We estimated the read noise as the standard deviation of pixel intensity in 1000 image frames acquired in full darkness with sufficiently brief exposure that the noise contribution from dark current was insignificant. To determine the dark current and dark signal non-uniformity, we captured 1000 frames in the dark, with sufficiently long exposure that read noise represented a fractionally insignificant contribution, and then averaged all the frames to yield a single image. We estimated the dark current and dark signal non-uniformity as the mean and standard deviation, respectively, of all pixels in the averaged image. These measurements and the basic electronic properties of the sensor enabled estimates of the sensor′s peak signal-to-noise-ratio and dynamic range (Supplementary Table 1), quantities that informed our simulations of microscope performance.

Data acquisition and control

The CMOS imager and LED PCBs were connected to a custom, external interface PCB for real-time data acquisition and control via nine fine and flexible wires encased together in a polyvinyl chloride (PVC) sheath of diameter ∼1.5 mm (Fig. 1). Seven of these wires interfaced to the image sensor, and the other two wires powered and controlled the LED. A two-wire Inter-Integrated Circuit (I^2C) serial communication interface enabled control of the camera. A Field-Programmable-Gate-Array (FPGA) chip, at the core of the interface PCB, provided the image sensor with a custom clock signal, which was synthesized from a quartz crystal oscillator, and acquired serial data output from the imager.

The image data was transferred from the camera to the FPGA over a Low-Voltage-Differential-Swing (LVDS) serial output interface, deserialized by the FPGA, and transferred to a computer through a USB-compatible data acquisition adapter PCB. An Electrically Erasable Programmable Read-Only Memory (EEPROM) flash chip permitted non-volatile storage of the FPGA configuration file, which automatically loaded into the FPGA at system power-up. This enabled plug-and-play operation of the microscope with real-time image acquisition and in-system camera control.

Brain imaging

The Stanford Administrative Panel on Laboratory Animal Care approved all procedures. We used male CD-1 wild type mice 7-14 weeks old and performed surgery using isoflurane (1.5–2.5%; mixed with 1–2 l/min O_2) anesthesia as previously described[6,9]. In brief, 1–6 days prior to imaging we exposed and cleaned the skull above cerebellum. (See Supplementary Note 1 regarding the hippocampal preparation). Using dental acrylic (Coltene/Whaledent, H00335) we fixed to the skull a custom metal plate allowing cranial access. On the imaging day, we opened a craniotomy (1.5–2.5 mm diameter; 6.5 mm posterior to bregma; 0.5 mm lateral) and irrigated the exposed tissue with warm artificial cerebral spinal fluid (ACSF; 125 mM NaCl, 5 mM KCl, 10 mM D-Glucose, 10 mM HEPES, 2 mM $MgSO_4$, 2 mM $CaCl_2$, pH adjusted to 7.4 with NaOH). To dampen heartbeat- and breathing-induced brain motion, we filled the craniotomy with agarose (2%; Type III-A, high EEO; Sigma) in ACSF and covered it with a coverslip fixed to the head plate, creating an optical window. We sealed the coverslip edges with dental acrylic. In Ca^{2+} imaging experiments, we left the dura intact for Ca^{2+} indicator injections but then removed it prior to agarose application.

In Ca^{2+} imaging studies, we labeled cerebellar cortex by multi-cell bolus-loading using the Ca^{2+}-indicator Oregon-Green-488-BAPTA-1-acetoxymethyl (OGB-1-AM)[6,9]. Concentrations of OGB-1-AM and DMSO in our pipette solution were 500 μM and 5%, respectively. In microcirculatory studies, we labeled the blood plasma by injection into a tail vein of 0.15–0.25 ml fluorescein-dextran (Sigma, FD2000S, 2000 kDa, 10 mg/ml)[6].

We positioned the miniature microscope above the optical window and lowered it towards the brain using a translation stage, until fluorescent surface structures were visible under weak illumination (90–200 μW). After locating a suitable recording site and focal depth, we turned the illumination off and fixed the microscope to the metal head plate using Cerebond™ adhesive (myNeuroLab.com, 39465030) and dental acrylic (Henry Schein, 5478203EZ). We allowed the mouse to recover from anesthesia before placing it into the behavioral arena. Imaging began once the mouse exhibited vigorous locomotor activity, typically 15-60 min after removal from isoflurane. To minimize the possibility of photo-induced alterations in physiology, the duration and mean power of continuous illumination were typically < 5 min and ∼170-600 μW at the specimen plane for each recording. There were at least 2 min between recordings, and the total recording duration was typically < 45 min. In Ca^{2+} imaging experiments, we assessed tissue health before and after imaging using an upright two-photon microscope equipped with a 20× water-immersion objective (Olympus, 0.95 NA, XLUMPlanFl) and an ultra-short pulsed Ti:sapphire laser (Tsunami,

Spectra-Physics) tuned to 800 nm. The frame acquisition rates of the integrated microscope were 100 Hz for studies of microcirculation and 30–46 Hz for Ca^{2+} imaging studies.

For studies of freely moving mice, we placed the mouse into a 45 cm × 45 cm × 15 cm arena made of transparent acrylic. A thin layer of bedding, a few food pellets, and an exercise wheel (Bio-Serv, K3250 and K3328) were inside the arena to provide a comfortable environment for the mouse. To record mouse behavior, we used either a video rate monochrome CMOS camera (Prosilica, EC640) with a high-resolution lens (Computar, M0814-MP2) situated above the arena or a video rate color CCD camera (Sony, DCR-VX2000NTSC) placed adjacent to the arena. We used two sets of infrared LED arrays (Lorex, VQ2120) for illumination with the overhead camera, but simply dim room lighting with the color camera.

Analysis of mouse behavior

During studies of cerebellar blood flow, we recorded the mouse's behavior within its arena using the overhead camera. To isolate information about the mouse's movements, we computed a movie of the behavioral arena containing only light intensity differences from the time-averaged image of the entire movie. Since the microscope housing appeared darker in these movies than any part of the mouse, we found the position of the mouse's head by setting to zero all pixels that were brighter than a threshold value and calculating the centroid of the remaining non-zero pixels that represented the microscope.

Using these data on the mouse's head position, we classified the animal's behavior in an automated way. We detected periods of wheel running when the mouse remained within a particular sub-region of the exercise wheel that could only be maintained when the mouse was running, and not stationary on the wheel. Mice never exhibited sustained walking on the exercise wheel, but did walk about the arena. We identified these walking periods when the mouse's speed was > 100 mm/s for at least 1 s outside the vicinity of the exercise wheel. Perhaps due to the relatively small size of the behavioral arena, the mice did not run when they were not on the wheel. We empiricially determined the values of all parameters used for these classification routines by carefully observing the videos of mouse behavior and comparing the results to manual scoring of behavior.

During neuronal Ca^{2+} imaging studies, we recorded the mouse's behavior using either the overhead or the color video cameras. In these studies we manually classified mouse behavior at 1 s increments into periods of quiet rest, small local movements (*e.g.* head movements, < 3 footsteps, body rotation), grooming, walking around the cage, running on the wheel, or other movements.

Basic image processing of brain imaging data

We performed all image processing using custom software written in MATLAB (Mathworks). Since the Bayer color filter on the CMOS image sensor blocked nearly all green fluorescence from reaching the sensor's red and blue pixels, we examined only the green pixels and created a re-sampled image whose rows corresponded to the green pixel diagonals of the raw data.

We then performed a rigid image registration to correct for lateral brain displacements by using an image registration algorithm implemented in the *ImageJ* plugin *TurboReg*[40]. We aligned each frame in a video sequence to a reference image that was the average image of the entire sequence. We also aligned the different video sequences from each experiment to each other. Corrections for lateral motion were typically < 1 μm.

In our later experiments we also corrected for fluctuations or drift in the illumination power provided by the LED (see *Illumination pathway*). We normalized each image frame by the estimate of illumination power calculated from the measured voltage drop across the LED. We calibrated the LED voltage-to-power conversion factor prior to imaging. In our earlier studies the LED voltage data were unavailable, and we omitted this step.

In our Ca^{2+} imaging studies, in which we were focused on neural synchrony at the ∼25-50 ms scale (Fig. 4), we corrected for the rolling shutter of the CMOS image sensor, which acquired the rows of each image sequentially rather than simultaneously. Within each image frame we assigned the sampling time of a row of pixels to be the frame integration time multiplied by the row index and divided by the total number of rows. In our studies of microcirculation this correction was unnecessary, because all computations of flow speed were performed using small neighborhoods of pixels over which the time differences in data acquisition were at the ∼1 ms scale or briefer, given that the interval between frames was 10 ms.

Analysis of microcirculatory dynamics

We determined erythrocyte flow speeds using a method based on temporal cross-correlations[6]. We first identified vessels by computing the standard deviation image of the raw data using all frames of the video. This computation highlighted vessels, which due to blood flow exhibited greater temporal fluctuations in intensity than background pixels[6]. We then chose measurement points randomly within the identified regions of vasculature.

To compute the speed of erythrocytes passing through a specific reference pixel, we computed the cross-correlation between the intensities of the reference pixel and neighboring pixels, for relative temporal delays, τ, of −1, 0, and +1 image frames[6]. For this calculation we used 10 s segments of data. We computed the centroid of each of the three cross-correlograms, and we determined the speed of erythrocytes passing through the reference pixel as the average of the distances between the $\tau = -1$ and the $\tau = +1$ centroids, divided by the time between two image frames. To track how a capillary's flow speed varied over time, we performed these calculations at 2 s increments over the entire duration of the movie data. To validate the accuracy of this automated algorithm, we have compared erythrocyte speeds as manually determined from the raw movie data to the speed values determined in an automated manner[33]. The two methods yielded close agreement[33] (r = 0.99); median differences between the two were 1.5%, and there were only a small minority of points where discrepancies were > 5%.

For each determination of a vessel's erythrocyte flow speed, we made a corresponding determination of vessel diameter. We computed cross-sectional profiles of the vessel's intensity along three parallel lines spaced one pixel apart within an image that was the

average of 2 s of data. The middle line passed through the reference pixel, and each of the three lines was perpendicular to the direction of flow. We then averaged the three line profiles and fit the result to a Lorentzian curve. We used the half-width at half-maximum (HWHM) of the fit as a measure of the vessel's diameter. We used Lorentzian fits, because we found empirically that Lorentzian curves provided superior approximations of vessels' profiles than Gaussians, which gave visible overestimates of vessel width.

Identification of Purkinje neurons

We identified spatial filters corresponding to individual Purkinje cell dendritic trees using an established approach to cell sorting[4] that sequentially applies principal component analysis (PCA) and then independent component analysis (ICA). For each experiment, to identify the Purkinje neurons we typically used 2000-2500 frames of imaging data during which the animal was awake but resting. We first reduced the dimensionality of this data by applying PCA and discarding the principal components that represented ongoing noise fluctuations, determined as in prior work[4]. We generally retained several hundred principal components in the data representation. Since each principal component generally represented a mixture of signals from multiple cells, we performed ICA on the principal components. As in prior work[4], from among the ICA spatial filters it was straightforward to identify spatial filters corresponding to the individual Purkinje cells, which were clearly distinguishable from those conveying noise. Using this combined PCA-ICA analysis we first examined a set of small regions ($\sim$120 × 80 pixels) that tiled the entire field of view. We then combined all of the identified cells into a single set while removing duplicates.

For display purposes only (Fig. 4a), we smoothed each spatial filter with a circularly symmetric gaussian filter (Matlab function conv2; standard deviation of 5 pixels) and then de-blurred the resultant with an ellipsoidal gaussian filter, with the long axis aligned along the medial-lateral dimension (Matlab function deconvlucy; standard deviations of 1 pixel and 6 pixels along the short and long axes, respectively). To delineate the cells' perimeters, we then thresholded the individual spatial filters at 20% of their maximum values.

Detection of Ca^{2+} spikes

We thresholded the identified spatial filter for each Purkinje neuron at 50% of its maximum value before extracting the [Ca^{2+}] related fluorescence trace. We then corrected for slow declines of fluorescence emissions as well as more rapid fluctuations in the fluorescence background, which were likely activity-induced. These two effects were separate from the fluctuations in LED illumination power. Slow declines of emissions were due to gradual bleaching of the Ca^{2+} indicator[9]. Activity-induced background fluctuations arose from the indicator's non-specific pattern of staining[4,9,20], which labeled not only Purkinje neurons but also other, out of focus neuronal fibers and processes.

To correct for these two effects, we tracked the mean percentage change in fluorescence within all pixels situated outside neurons, denoted $\Phi(t)$, as a measure of background fluctuations. $\Phi(t)$ was typically within [–5%, +10%]. We corrected each full frame, $F(t)$, by creating a new image, $F'(t)$, where $F'(t) = F(t) – \Phi(t)*F_0$, where F_0 is the time-averaged mean image of stack $F(t)$. Fluorescence fluctuations in areas outside neurons were much

reduced within $F'(t)$. This also facilitated detection of Purkinje neurons' Ca^{2+} spikes, since the neuronal areas had likewise been corrected for bleaching and the out of focal plane fluctuations.

We performed algorithmic spike detection on the $F'(t)$ traces by applying a temporal deconvolution with a decaying exponential of 150 ms time constant[41], applying a high-pass filter (8-pole Butterworth; –3 dB cutoff frequency of 8 Hz) and marking as spikes all positive-going threshold crossings at their local maximum. For each video recording, a spike detection threshold was chosen for each neuron so that false positives would occur at a rate <0.05 Hz, which is ∼2.5% −10% of Purkinje neurons' typical Ca^{2+} spike rates and comparable to prior percentages of false positive Ca^{2+} spike detection in these cells[4,6,20]. To estimate the rate of false positive detection, we examined 20 fluorescence traces generated from independent sets of randomly chosen pixels. The number of pixels randomly sampled for each trace was set equal to the mean number of pixels within the neurons' spatial filters for that experiment.

The pairwise correlation coefficient for two cells was defined as Pearson's correlation coefficient, the covariance in the activity between the two spike trains divided by the product of their standard deviations. This yielded a correlation coefficient within [-1,1].

Detection of synchronous microzonal activity

We classified Purkinje neurons into clusters (Fig. 4a,c) of cells based on their pairwise correlations by using *k*-means cluster analysis. We set *k* in each experiment to match the number of blocks in the pairwise correlation matrices, which we and others have found to have a block-diagonal form[4,20,22]. We interpreted each cluster of neurons as a microzone. To verify that synchronous activity was essential to identification of microzones, we temporally shuffled the data by shifting each neuron's trace by a randomly chosen time increment. This preserved all temporal structure within individual traces but disrupted concerted activity between neurons. We found no microzones after shuffling. We computed event trains in binary format to represent the concerted dynamics of the microzones. In these event trains, each time bin was assigned a value of 0, unless 50% or more of the visible cells within the microzone exhibited synchronous spiking, in which case the value was 1 (closed symbols in Fig. 5a–e). We also calculated event traces using a weaker definition of synchrony, in which 35% or more of the visible cells within a microzone exhibited synchronous spiking (open symbols in Fig. 5a–e).

Using an algorithm based on a modified version of theMATLAB routine nchoosek(), we computed the expected rates of synchronized microzonal activation based on the empirically determined spike rates for each neuron and the null hypothesis that the individual neurons' dynamics were independent. The measured rates were $\sim 10^{10}$ and $\sim 10^{5}$ times greater than the expected rates, under the respective criteria that > 50% or > 35% neurons within a microzone must fire concurrently for an event to qualify as synchronized activity.

Statistical analysis—We performed all statistical tests in MATLAB (Mathworks) using non-parametric methods, with the exception of the likelihood ratio tests, which assume binomial distributions.

Supplementary Material

Refer to Web version on PubMed Central for supplementary material.

Acknowledgments

We thank E.J. Baron, S.S. Gambhir, E.T.W. Ho, R. Luo, E. Mukamel, J. Perlin, L. Sasportas, W. Talbot, and the Stanford Varian machine shop for technical assistance. We thank L. Looger of the HHMI Janelia Farm Research Campus for the gift of GCaMP3 plasmid. We gratefully acknowledge graduate fellowships from the National Science Foundation and Stanford University (LDB), postdoctoral fellowships from the Human Frontier Science Program (AN) and the Machiah Foundation (YZ), and research funding to MJS from Lawrence Livermore National Laboratory, the Office of Naval Research, the National Institutes of Health Nanomedicine Development Center for Optical Control of Biological Function, the National Science Foundation Center for Biophotonics, the Packard and the Paul G. Allen Family Foundations, and the Stanford University *CNC* Program.

References

1. Arthur, WB. The Nature of Technology: What It Is and How It Evolves. 2009. Free Press
2. Wilt BA, et al. Advances in light microscopy for neuroscience. Annu Rev Neurosci. 2009; 32:435–506. [PubMed: 19555292]
3. Helmchen F, Fee M, Tank D, Denk W. A miniature head-mounted two-photon microscope: high-resolution brain imaging in freely moving animals. Neuron. 2001; 31:903–912. [PubMed: 11580892]
4. Mukamel EA, Nimmerjahn A, Schnitzer MJ. Automated analysis of cellular signals from large-scale calcium imaging data. Neuron. 2009; 63:747–760. [PubMed: 19778505]
5. Dombeck DA, Khabbaz AN, Collman F, Adelman TL, Tank DW. Imaging large-scale neural activity with cellular resolution in awake, mobile mice. Neuron. 2007; 56:43–57. [PubMed: 17920014]
6. Flusberg BA, et al. High-speed, miniaturized fluorescence microscopy in freely moving mice. Nat Methods. 2008; 5:935–938. [PubMed: 18836457]
7. Sawinski J, et al. Visually evoked activity in cortical cells imaged in freely moving animals. PNAS. 2009
8. Andermann ML, Kerlin AM, Reid RC. Chronic cellular imaging of mouse visual cortex during operant behavior and passive viewing. Front Cell Neurosci. 2010; 4:3. [PubMed: 20407583]
9. Nimmerjahn A, Mukamel EA, Schnitzer MJ. Motor behavior activates Bergmann glial networks. Neuron. 2009; 62:400–412. [PubMed: 19447095]
10. Hayden EC. Microscopic marvels: Microscope for the masses. Nature. 2009; 459:632–633. [PubMed: 19494890]
11. Rogers JD, et al. Imaging performance of a minature integrated microendoscope. J Biomedical Optics. 2008; 13 054020(054021)-054020(054026).
12. Breslauer DN, Maamari RN, Switz NA, Lam WA, Fletcher DA. Mobile phone based clinical micrscopy for global health applications. PLoS ONE. 2009; 4:1–7.
13. Cui X, et al. Lensless high-resolution on-chip optofluidic microscopes for Caenorhabditis elegans and cell imaging. PNAS. 2008; 105:10670–10675. [PubMed: 18663227]
14. Seo S, Su T, Tseng DK, Erlinger A, Ozcan A. Lensfree holographic imaging for on-chip cytometry and diagnostics. Lab On a Chip. 2009; 9:777–787. [PubMed: 19255659]
15. El Gamal A, Eltoukhy H. CMOS image sensors. IEEE Circuits and Device Magazine. 2005; 21:6–20.
16. Andersson G, Armstrong DM. Complex Spikes in Purkinje-Cells in the Lateral Vermis (B-Zone) of the Cat Cerebellum during Locomotion. Journal of Physiology-London. 1987; 385:107–134.
17. Leicht R, Schmidt RF. Somatotopic Studies on Vermal Cortex of Cerebellar Anterior Lobe or Unanesthetized Cats. Experimental Brain Research. 1977; 27:479–490. [PubMed: 856618]
18. Jorntell H, Ekerot C, Garwicz M, Luo XL. Functional organization of climbing fibre projection to the cerebellar anterior lobe of the rat. J Physiol. 2000; 522(Pt 2):297–309. [PubMed: 10639105]

19. Glickstein M, Sultan F, Voogd J. Functional localization in the cerebellum. Cortex. 2009
20. Ozden I, Lee HM, Sullivan MR, Wang SS. Identification and clustering of event patterns from in vivo multiphoton optical recordings of neuronal ensembles. J Neurophysiol. 2008; 100:495–503. [PubMed: 18497355]
21. Raymond JL, Lisberger SG, Mauk MD. The cerebellum: a neuronal learning machine? Science. 1996; 272:1126–1131. [PubMed: 8638157]
22. Ozden I, Sullivan MR, Lee HM, Wang SS. Reliable coding emerges from coactivation of climbing fibers in microbands of cerebellar Purkinje neurons. J Neurosci. 2009; 29:10463–10473. [PubMed: 19710300]
23. Apps R, Garwicz M. Anatomical and physiological foundations of cerebellar information processing. Nat Rev Neurosci. 2005; 6:297–311. [PubMed: 15803161]
24. Lyons DA, et al. erbb3 and erbb2 are essential for Schwann cell migration and myelination in zebrafish. Current Biology. 2005; 15:513–524. [PubMed: 15797019]
25. Pogoda HM, et al. A genetic screen identifies genes essential for development of myelinated axons in zebrafish. Dev Biol. 2006; 298:118–131. [PubMed: 16875686]
26. Pepperkok R, Ellenberg J. High-throughput fluorescence microscopy for systems biology. Nat Rev Mol Cell Biol. 2006; 7:690–696. [PubMed: 16850035]
27. Kachouie N, Kang L, Khademhosseini A. Arraycount, an algorithm for automatic cell counting in microwell arrays. Biotechniques. 2009; 47:x–xvi. [PubMed: 19852758]
28. Brinkmann M, Lutkemeyer D, Gudermann F, Lehmann J. New technologies for automated cell counting based on optical image analysis; bThe Cellscreen'. Cytotechnology. 2002; 38:119–127. [PubMed: 19003093]
29. Stone LR, Gray DR, Remple KL, Beaudet MP. Accuracy and precision comparison of the hemocytometer and automated cell counting methods. FASEB J. 2009; 23_MeetingAbstracts:827.
30. Steingart KR, et al. Fluorescence versus conventional sputum smear microscopy for tuberculosis: a systematic review. Lancet Infect Dis. 2006; 6:570–581. [PubMed: 16931408]
31. Engelbrecht CJ, Johnston RS, Seibel EJ, Helmchen F. Ultra-compact fiber-optic two-photon microscope for functional fluorescence imaging in vivo. Opt Express. 2008; 16:5556–5564. [PubMed: 18542658]
32. Murari K, Etienne-Cummings R, Cauwenberghs G, Thakor N. An integrated imaging microscope for untethered cortical imaging in freely-moving animals. Conf Proc IEEE Eng Med Biol Soc. 2010; 2010:5795–5798. [PubMed: 21097102]
33. Barretto RP, et al. Time-lapse imaging of disease progression in deep brain areas using fluorescence microendoscopy. Nat Med. 2011; 17:223–228. [PubMed: 21240263]
34. Tian L, et al. Imaging neural activity in worms, flies and mice with improved GCaMP calcium indicators. Nat Methods. 2009; 6:875–881. [PubMed: 19898485]
35. Carey RM, Verhagen JV, Wesson DW, Pirez N, Wachowiak M. Temporal structure of receptor neuron input to the olfactory bulb imaged in behaving rats. J Neurophysiol. 2009; 101:1073–1088. [PubMed: 19091924]
36. Jung JC, Mehta AD, Aksay E, Stepnoski R, Schnitzer MJ. In vivo mammalian brain imaging using one- and two-photon fluorescence microendoscopy. J Neurophysiol. 2004; 92:3121–3133. [PubMed: 15128753]
37. Murayama M, et al. Dendritic encoding of sensory stimuli controlled by deep cortical interneurons. Nature. 2009; 457:1137–1141. [PubMed: 19151696]
38. Welsh JP, Lang EJ, Suglhara I, Llinas R. Dynamic organization of motor control within the olivocerebellar system. Nature. 1995; 374:453–457. [PubMed: 7700354]
39. Barretto RP, Messerschmidt B, Schnitzer MJ. In vivo fluorescence imaging with high-resolution microlenses. Nat Methods. 2009; 6:511–512. [PubMed: 19525959]
40. Thevenaz P, Ruttimann UE, Unser M. A pyramid approach to subpixel registration based on intensity. IEEE Trans Image Process. 1998; 7:27–41. [PubMed: 18267377]
41. Yaksi E, Friedrich RW. Reconstruction of firing rate changes across neuronal populations by temporally deconvolved Ca2+ imaging. Nat Methods. 2006; 3:377–383. [PubMed: 16628208]

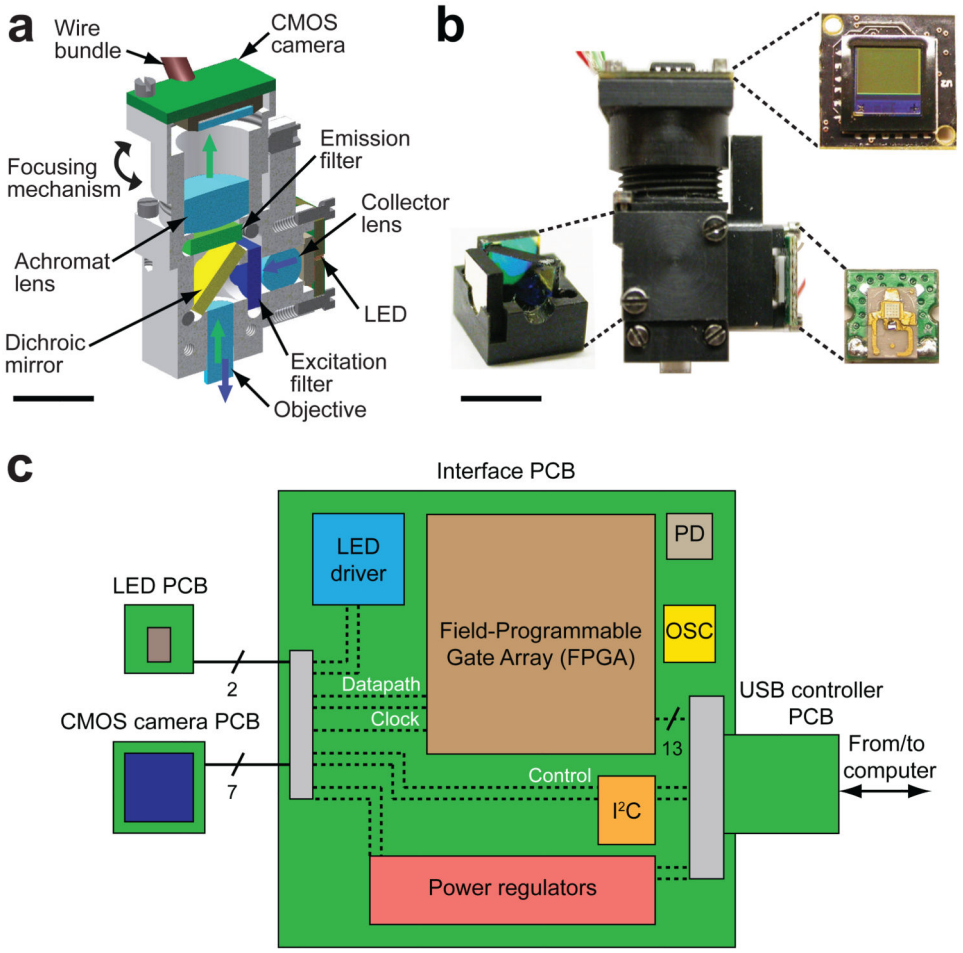

Figure 1. Design and fabrication of an integrated fluorescence microscope

a. Computer-assisted design of an integrated microscope, shown in cross-section. Blue and green arrows mark illumination and emission pathways, respectively. Scale bar is 5 mm.

b. Assembled integrated microscope. Insets show, clockwise from bottom left: filter cube holding dichroic mirror and excitation and emission filters; printed circuit board (PCB) holding the complementary metal-oxide-semiconductor (CMOS) camera chip; PCB holding the light emitting diode (LED) illumination source. The wire bundles for LED and CMOS boards are visible. Scale bar is 5 mm and applies to all four photographs.

c. Electronics for real-time image acquisition and control. The LED and CMOS sensoreach have their own PCB. These boards are connected to a custom, external PCB via nine fine wires (two to the LED and seven to the camera) encased in a single polyvinyl chloride sheath. The external PCB interfaces with a computer via a USB adaptor board. Labeled components summarize circuitry for providing power, controlling the LED and CMOS camera, and transferring data. Abbreviations: PD, flash programming device; OSC, Quartz crystal oscillator; I^2C, Two-wire Inter-Integrated Circuit serial communication interface.

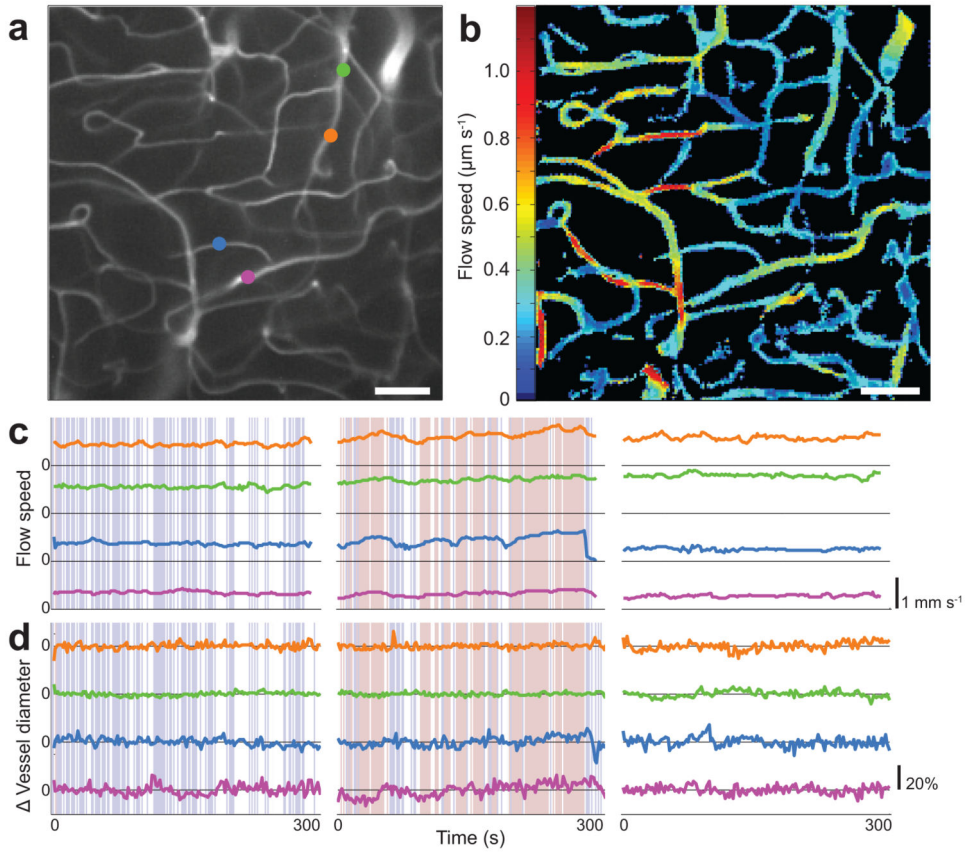

Figure 2. Cerebellar microcirculatory dynamics in freely behaving mice

a. Microvasculature in cerebellar cortex of a freely behaving mouse, after intravascular injection of fluorescein-dextran dye. The image shown (300 × 300 pixels; 440 μW illumination power at the specimen plane) is the standard deviation of a 10 s movie, a computation that highlights vasculature (**Online Methods**). Colored dots mark the locations of corresponding measurements in (**c, d**). Scale bar is 50 μm.

b. Map of erythrocyte flow speeds averaged over an interval of 30 s for vessels of (**a**). Scale bar is 50 μm.

c, d. Erythrocyte flow speeds, (**c**), and vessel diameter changes, (**d**), for the 4 vessels marked in (**a**). Blue shading marks periods of movement about the cage. Red shading indicates running on an exercise wheel. White shading marks when the mouse rested orbarely moved. Black vertical lines separate different records from the same mouse and specimen field.

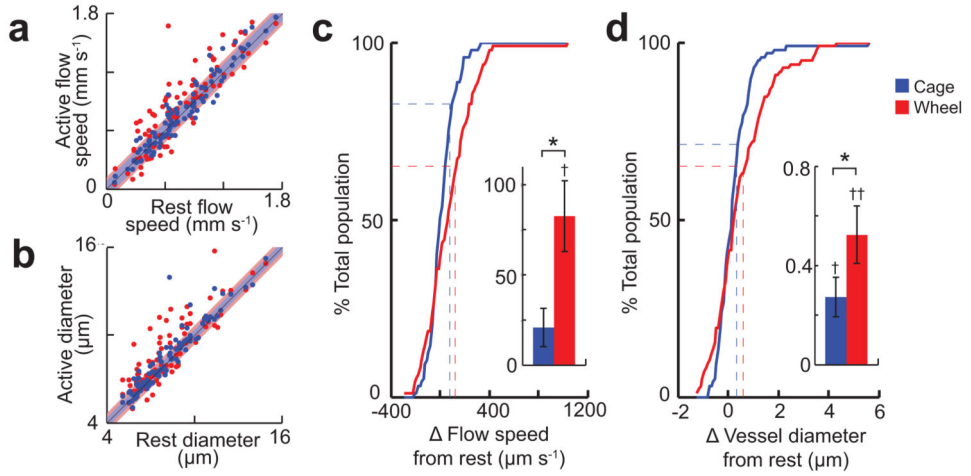

Figure 3. Non-uniform regulation of cerebellar capillaries during locomotion

a, b. Erythrocyte speeds, (**a**), and vessel diameters, (**b**), compared between rest and locomotion. Each datum represents a vessel location in the vermis. Data above the diagonal indicate up-regulation in speed or diameter during motor activity (blue points, walking within the cage; red points, wheel running). Shaded blue and red areas demarcate 1 s.d. of measurement fluctuations calculated using the data below the diagonal.

c. Cumulative histogram of changes in flow speeds during walking about the cage (blue) or wheel running (red), compared to rest. Histogram portions above and to the right of areas enclosed by colored dashed lines represent data for vessel locations lying above the color corresponding shaded areas in (**a**). (**Inset**) Mean ± s.e.m. changes compared to rest. (*) Indicates significant difference between walking and running ($P = 4 \cdot 10^{-5}$); (†) indicates significant difference from rest ($P = 2 \cdot 10^{-4}$), using Wilcoxon signed-rank tests.

d. Cumulative histogram of changes in vessel diameters during walking (blue) or running (red), compared to rest. Histogram portions outside areas enclosed by colored dashed lines represent measurements lying above the corresponding shaded areas in (**b**). (**Inset**) Mean ± s.e.m. changes. (*) Indicates significant difference between walking and running ($P = 6 \cdot 10^{-3}$); (†) and (††) indicate significant differences from rest of $P = 1 \cdot 10^{-3}$ and $P = 1 \cdot 10^{-4}$, respectively, using Wilcoxon signed-rank tests.

Data in (**a–d**) comprise $n = 97$ vessel locations from 3 mice.

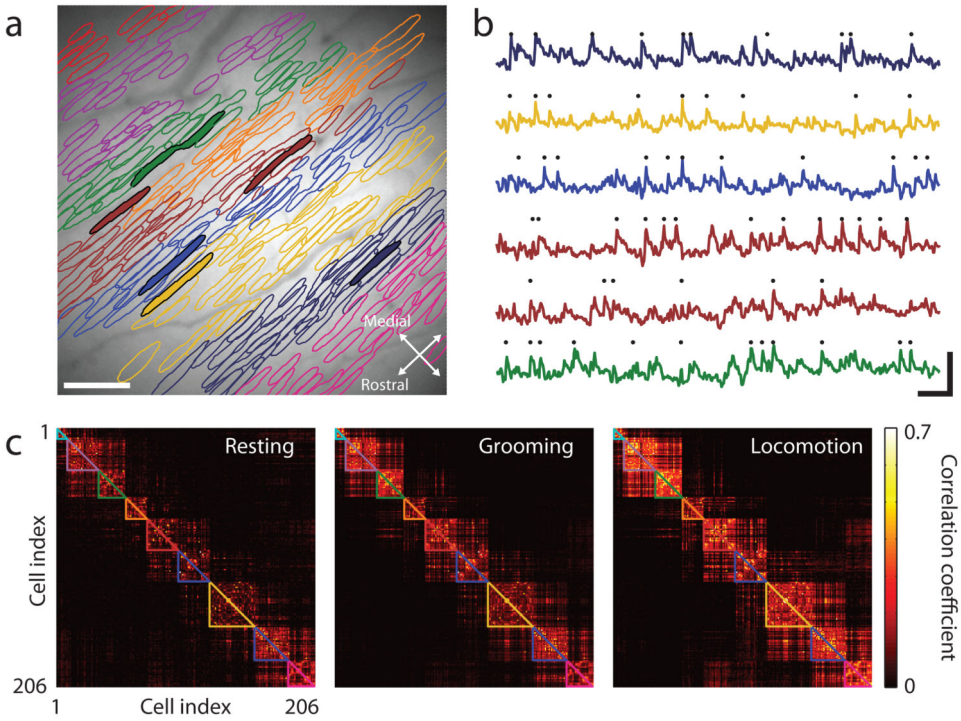

Figure 4. Purkinje neurons' Ca^{2+} spiking dynamics during motor behavior

a. Contours of 206 Purkinje neurons identified in a freely behaving mouse, super imposed on a time-averaged fluorescence image (480 × 480 pixels; 170-250 μW illumination at the specimen plane) of the cerebellar surface after injection of the Ca^{2+}-indicatorOregeon-Green-BAPTA-1-AM. Each color indicates one of nine identified microzones. Filled contours mark neurons whose activity is shown in (**b**). Scale bar is 100 μm.

b. Relative changes in fluorescence (Δ*F*/*F*) from filled neurons in (**a**). Black dots mark detected Ca^{2+} spikes. Scale bars: 1 s (horizontal); 3% Δ*F*/*F* (vertical).

c. Spike train correlation coefficients for pairs of neurons, during resting, grooming, and locomotion. Colored outlines indicate microzones identified by cluster analysis of the correlation coefficients and correspond to those in (**a**).

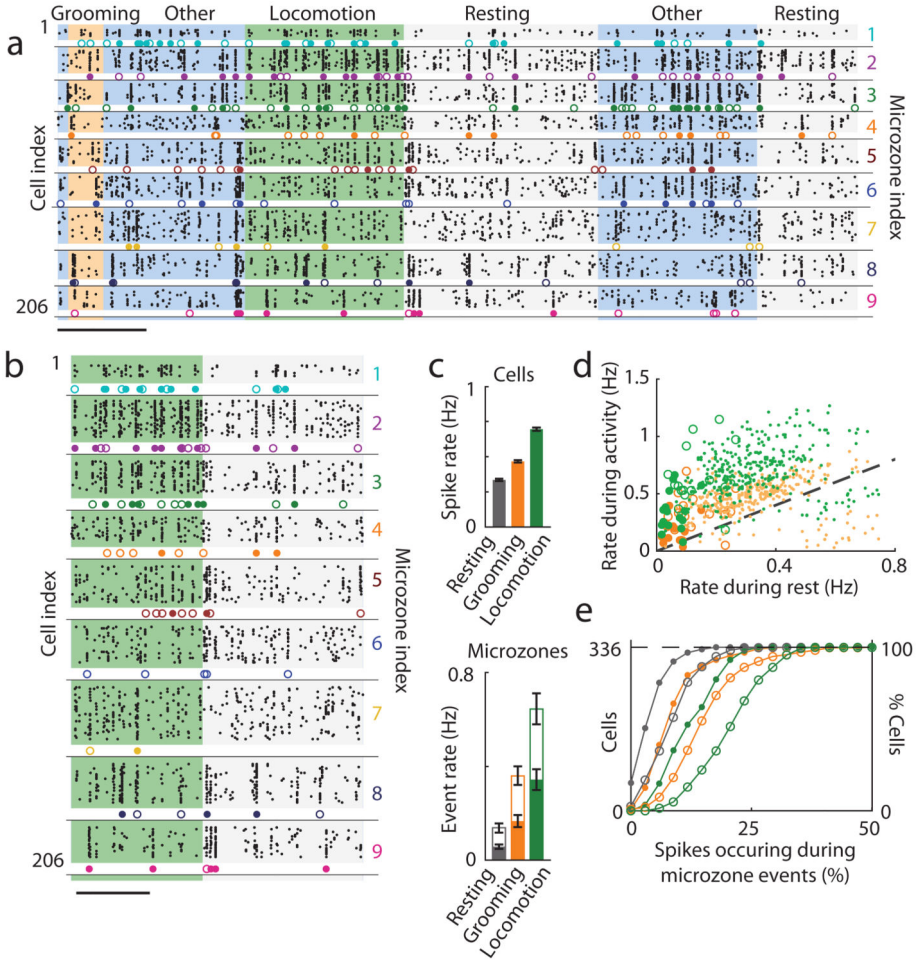

Figure 5. Cerebellar microzones exhibit large-scale, synchronized Ca^{2+} spiking during motor behavior

a. Ca^{2+} spike (black dots) raster plots for neurons of Fig. 4a. Colored shading indicates the mouse's behavior (peach, grooming; green, locomotion; gray, resting; other small movements, blue). Microzone rasters (colored dots) show Ca^{2+} spiking by > 35% (open dots) or > 50% (closed dots) of neurons identified in each microzone. Scale bar is 5 s.

b. Expanded view of the locomotion and first resting periods of (**a**). Scale bar is 5 s.

c. Mean ± s.e.m rates of individual neuronal spiking (*top*) and synchronized microzone activation (*bottom*: > 35% cells synchronized, unfilled bars; > 50% cells, solid bars).

d. Spike rates for individual cells (small data points) and synchronized microzonal activation (> 35% cells, large open points; > 50% cells, large solid points) plotted for periods of grooming *vs*. rest (yellow points) or locomotion *vs*. rest (green points).

e. Cumulative histograms of percentages of cell's spikes occurring during synchronized activation (> 35% activation, open points; > 50% activation, solid points; locomotion, green; grooming, yellow; resting, gray).

Data of (**c-e**) are from *n* = 3 mice, 336 cells, and 16 microzones.

Table 1

Comparison of the integrated microscope to a recent fiber-bundle based fluorescence microscope[6]

Fluorescence throughput is defined here as the efficiency with which captured fluorescence emissions are relayed from the specimen plane to the detection plane. Given the comparable numerical apertures (∼0.5) and sensor quantum efficiencies, the five-fold difference in fluorescence throughput is the chief reason the integrated microscope has far greater sensitivity.

	Integrated microscope	Fiber-bundle microscope[6]
Nyquist detection resolution	∼2.5 μm	∼2.8-3.9 μm
Optical resolution	∼1.5 μm	∼2.8-3.9 μm
Detection-limited field of view	0.48 mm^2	0.07 mm^2
Optical field-of-view	1 mm^2	0.07 mm^2
Fluorescence throughput to sensor	∼95%	∼20%
Signal transmission	Digital image data	Fluorescence photons
Mechanical tether to animal	Floppy	Deflection-dependent stress
Reference frame of optics	All optics move with animal	Lamp, camera stay in laboratory frame
Illumination field at specimen	Does not rotate	Rotates with animal movement
Portability of optics	Fit in wallet or purse	Benchtop instrument on air table
Total system portability	Briefcase compatible	Benchtop instrument on air table
Portability of optical function	No re-alignment needed	Optical re-alignment needed
Cost of optoelectronic parts	∼$1-10	∼$25,000-50,000
Manufacturing scalability	Mass producible	No batch fabrication for lamp, camera